ARTICLE

Application of Hankel Dynamic Mode Decomposition for Wide Area Monitoring of Subsynchronous Resonance

Lei Wang[1], Tiecheng Li[1], Hui Fan[2], Xuekai Hu[1], Lin Yang[3] and Xiaomei Yang[3,*]

[1]State Grid Hebei Electric Power Research Institute, Shijiazhuang, 050021, China

[2]State Grid Hebei Electric Power Company, Shijiazhuang, 050021, China

[3]The College of Electrical Engineering, Sichuan University, Chengdu, 610065, China

*Corresponding Author: Xiaomei Yang. Email: yangxiaomei@scu.edu.cn

ABSTRACT

In recent years, subsynchronous resonance (SSR) has frequently occurred in DFIG-connected series-compensated systems. For the analysis and prevention, it is of great importance to achieve wide area monitoring of the incident. This paper presents a Hankel dynamic mode decomposition (DMD) method to identify SSR parameters using synchrophasor data. The basic idea is to employ the DMD technique to explore the subspace of Hankel matrices constructed by synchrophasors. It is analytically demonstrated that the subspace of these Hankel matrices is a combination of fundamental and SSR modes. Therefore, the SSR parameters can be calculated once the modal parameter is extracted. Compared with the existing method, the presented work has better dynamic performances as it requires much less data. Thus, it is more suitable for practical cases in which the SSR characteristics are time-varying. The effectiveness and superiority of the proposed method have been verified by both simulations and field data.

KEYWORDS

Hankel; dynamic mode decomposition; time-varying; sub-synchronous oscillation; synchrophasor

Nomenclature

f_s	frequency of subsynchronous component
α_s	damping of subsynchronous component
A_s	amplitude of subsynchronous component
f_1	frequency of fundamental component
A_1	amplitude of fundamental component
f_r	reporting frequency for PMU
X_p	synchrophasor provided in PMU
X_c	reported synchrophasor

1 Introduction

The fast growth and application of doubly-fed induction generators (DFIGs) in series compensated systems have significantly increased the occurrence of subsynchronous resonance (SSR) [1]. Recent SSR events in south Texas of USA [2] and North China [3,4] indicated that the oscillation could be system-wide which involves complex interactions among grid components. It is thus of great importance to provide a wide area monitoring of SSR parameters, including the magnitude, frequency and damping. The data are crucial for replicating SSR events, identifying the sources of SSR [5] and supporting the design of countermeasures, e.g., feedback-linearized sliding mode controller [6], energy-shaping L2-gain controller [7], damping controller [8].

To date, two types of data have been considered for SSR parameter identification (SSRPI). One is the waveform data provided by the fault recorder. This type of data contains the complete information of the oscillation and thus can be easily utilized for SSRPI through various signal-processing algorithms, such as Prony [9] and the recursive least square (RLS) method [10]. Additionally, model decomposition-based techniques, such as the Hilbert-Huang transform [11] and variational mode decomposition (VMD) [12], can perform parameter identification decomposition after the time signals are decomposed into multifrequency mode components. Unfortunately, the fault recorder is locally stored, and whether it records the SSR data depends on the triggering mechanism. This deficiency imposes great challenges for wide area monitoring or system-wide analysis [13].

Another option is to take advantage of the synchrophasors provided by the wide area monitoring system (WAMS). Currently, phasor measurement units (PMUs) have been widely deployed in transmission networks [14], making the WAMS a promising platform for SSR monitoring. The main challenge here is that the synchrophasor only captures the fundamental phasors. As a result, the SSR components will appear as the spectral leakage components. Studies have been conducted to address this issue. The work in [15] demonstrated that it is possible to identify the SSR frequency from synchrophasors. Recently, some modal parameter extraction methods, e.g., classic Prony analysis, estimation of signal parameters via the rotational invariance technique (ESPRIT) and the matrix pencil method [16], have been developed to extract the SSO parameters. In addition, the recent study in [17] further proposed a DFT-based correction method to recover the SSR amplitude from spectral leakage components. An interpolated DFT (InpDFT)-based method was also proposed in [13] to achieve better identification accuracy through the consideration of damping parameters.

However, the DFT-based methods rely on a long data window to obtain better accuracy for estimating the SSR parameters and assume that these parameters are constant within the window. In practice, the SSR parameters are usually time-varying due to the stochastic nature of wind resources and the volatile operation conditions of the grid [3]. When a short window is used in DFT-based methods for analyzing nonstationary signals, the spectrum of the SSR component in the synchrophasors will be significantly affected by spectral leakage from the fundamental frequency phasors. In this way, large estimation errors are unavoidable.

Within this context, this paper proposes a signal analysis technique based on dynamic mode decomposition (DMD). DMD seeks a linear dynamic operator to best approximate the underlying dynamics of the system. Its performance has been found to be satisfactory in a wide variety of applications, including fluid communities [18], biomedical fields [19] and power system areas. As an example, the work in [20] successfully applied DMD for spatiotemporal PMU data to monitor low-frequency oscillations.

In this paper, we implemented the key parameter estimation of SSR by using the DMD method from the eigenvalues of Hankel matrices after the behavior of the synchrophasors under SSR is

analyzed. The contributions of this paper include the following: (1) temporal synchrophasors with less data (less than 1 s) are used to construct two Hankel matrices, and the computational efficiency is improved. Note that only a single channel of measurement is required here. (2) The DMD method is performed on two Hankel matrices to estimate the parameters of SSR, and the number of dominant modes is automatically determined rather than predetermined; thus, the dynamic performance of SSR is captured well. (3) The proposed method is performed on simulation and field data, demonstrating the effectiveness of the proposed method.

The remainder of the paper is organized as follows. Section 2 analyzes the behavior of synchrophasors under SSR and defines the DMD problem to be solved. The Hankel-DMD method is explained in Section 3 for the identification of SSR components. Section 4 verifies the effectiveness of the proposed method by using simulation data and field data under dynamic and noisy conditions. A comparative study is also conducted to show the superiority of the proposed method.

2 Synchrophasor Model under SSR

This paper focuses on the SSR caused by the interaction between DFIGs and series-compensated systems. For such cases, all wind farms and the network are engaged in one SSR mode [3,4,21]. As a result, the current waveform data in the time domain under SSR can be expressed as

$$x(t) = A_1 \cos(2\pi f_1 t + \phi_1) + A_s e^{\alpha_s t} \cos(2\pi f_s t + \phi_s) \tag{1}$$

where α_s is the damping factor of SSR and (A_1, f_1, ϕ_1) and (A_s, f_s, ϕ_s) are amplitudes, frequencies and initial phases of the fundamental and SSR components, respectively. With a fixed sampling frequency f_p, the signal $x(t)$ in (1) is sampled as $x(n)$, expressed as

$$x(n) = A_1 \cos\left(2\pi \frac{f_1}{f_p} n + \phi_1\right) + A_s e^{\frac{\alpha_s}{f_p} n} \cos\left(2\pi \frac{f_s}{f_p} n + \phi_s\right) \tag{2}$$

Commonly, synchrophasors are obtained by applying a discrete Fourier transform (DFT) on $x(n)$ within a rectangle window. The length of the window is $N_p = f_p/f_0$, and f_0 is the nominal frequency, i.e., 50 or 60 Hz. Based on the Euler equation and series summation, the DFT spectra at the pth sliding time window can be derived as

$$X(p, k) = X_1^+(p, k) + X_1^-(p, k) + X_s^+(p, k) + X_s^-(p, k)$$
$$p = 1, 2, \ldots, \quad k = 0, 1, \ldots, N_p - 1 \tag{3}$$

where $\left(X_1^+(p, k), X_1^-(p, k)\right)$ and $\left(X_s^+(p, k), X_s^-(p, k)\right)$ are the positive and negative spectra of the fundamental and SSR components, respectively, and k is the spectral bin number.

Let $f_{p1} = f_1/f_p = L_1/N_p$, $\alpha_{ps} = \alpha_s/f_p = \hat{\alpha}_{ps}/N_p$ and $f_{ps} = f_s/f_p = L_s/N_p$, where L_1 and L_s are the normalized f_1 and f_s expressed in spectral bins, respectively, and $\hat{\alpha}_{ps}$ is the normalized damping ratio $\hat{\alpha}_s$. We compute $X_1^{\pm}(p, k)$ and $X_s^{\pm}(p, k)$ as

$$\begin{cases} X_1^+(p, k) = A_1 C_1 (L_1 - k) e^{j(2\pi p f_{p1} + \phi_1)} \\ X_1^-(p, k) = A_1 C_1^* (L_1 + k) e^{-j(2\pi p f_{p1} + \phi_1)} \\ X_s^+(p, k) = A_s C_s (L_s - k) e^{j(2\pi p f_{ps} - jr\alpha_{ps} + \phi_s)} \\ X_s^-(p, k) = A_s C_s^* (L_s + k) e^{-j(2\pi p f_{ps} + jr\alpha_{ps} + \phi_s)} \end{cases} \tag{4}$$

with

$$
\begin{cases}
C_1(s) = \dfrac{1}{2N_p} \times \dfrac{1 - e^{j2\pi s}}{1 - e^{(j2\pi s / N_p)}}, \\[2mm]
C_s(s) = \dfrac{1}{2N_p} \times \dfrac{1 - e^{(\hat{\alpha}_{ps} + j2\pi s)}}{1 - e^{(\hat{\alpha}_{ps} + j2\pi s)/N_p}},
\end{cases}
\tag{5}
$$

where $(.)^*$ is the conjugate transpose operator, C_1 represents the spectral leakage on the synchrophasors, considering that there is a frequency deviation between f_1 and f_0, and C_s represents the spectral leakage factor of the SSR component on the synchrophasors. Since we can only obtain $A_s C_1$ from the measured synchrophasor data, C_s is the key parameter for estimating A_s.

At the pth data window, the synchrophasor $X_p(p)$ in the PMUs is obtained as the 2nd spectral.

bin (i.e., $k = 1$) of the spectrum X in (3), expressed as

$$
X_p(p) = X_1^+(p, 1) + X_1^-(p, 1) + X_s^+(p, 1) + X_s^-(p, 1)
\tag{6}
$$

Assuming that f_1, f_s and α_s do not change significantly in a short time window, we regard $C_1(L_1 - 1)$ and $C_1^*(L_1 + 1)$ in (4) as constants at a certain f_1 and regard $C_s(L_s - 1)$ and $C_s^*(L_s + 1)$ as constants at a certain α_s and f_s.

Generally, a series of X_p provided by the PMUs are transmitted to the main station with a certain reporting frequency $f_r (= 1/T_r$, where T_r is the reporting interval time), typically 50 or 100 Hz for 50 Hz systems. Then, the reported synchrophasor X_c is obtained by resampling X_p with the interval $f_{pr} = f_r/f_p$ as $X_c(m) = [X_p(0), \dots, X_p(mf_{pr} - 1)]$, $(m = 0, 1, \dots)$. Accordingly, X_c should be expressed by replacing the variable p in (6) with mf_{pr}, as shown in (7):

$$
\begin{aligned}
X_c(m) = & A_1 C_1(L_1 - 1) e^{j(\omega_{r1} m + \phi_1)} + A_1 C_1^*(L_1 + 1) e^{-j(\omega_{r1}^* m + \phi_1)} \\
& + A_s C_s(L_s - 1) e^{j(\omega_{rs} m + \phi_s)} + A_s C_s^*(L_s + 1) e^{-j(\omega_{rs}^* m + \phi_s)}
\end{aligned}
\tag{7}
$$

with

$$
\omega_{r1} = 2\pi f_1 T_r, \qquad \omega_{rs} = 2\pi f_s T_r - j\alpha_s T_r
\tag{8}
$$

where ω_{r1} and ω_{rs} are the normalized radial frequencies of the fundamental and SSR components related to T_r, respectively.

By defining

$$
\begin{cases}
a_1 = A_1 C_1(L_1 - 1) e^{j\phi_1}, a_2 = A_1 C_1^*(L_1 + 1) e^{-j\phi_1} \\
a_3 = A_s C_s(L_s - 1) e^{j\phi_s}, a_4 = A_s C_s(L_s + 1) e^{-j\phi_s}
\end{cases}
\tag{9}
$$

and

$$
\begin{cases}
\lambda_1 = e^{j\omega_{r1}}, \lambda_2 = \lambda_1^* \\
\lambda_3 = e^{j\omega_{rs}}, \lambda_4 = \lambda_3^*
\end{cases}
\tag{10}
$$

we rewrite (7) as

$$
X_c(m) = a_1 \lambda_1^m + a_2 \lambda_2^m + a_3 \lambda_3^m + a_4 \lambda_4^m,
\tag{11}
$$

which denotes that X_c under SSR is a linear combination of four distinct modes, i.e., (λ_1, λ_2) from the fundamental component and (λ_3, λ_4) from the SSR component. Generally, there are q frequency components in (11), and we generalize (11) as

$$
X_c(m) = a_1 \lambda_1^m + \dots + a_r \lambda_r^m
\tag{12}
$$

where $r = 2q$. When SSR does not occur, $r = 2$, while when SSR occurs, $r = 4$, as shown in (11).

Eq. (12) indicates that the synchrophasors under SSR are a linear combination of four phasors rotating at different frequencies. The index λ_i thus can be approached by the Hankel-DMD method using a series of synchrophasors. Once λ_i is known, the frequency f_s and damping of the SSR can be calculated according to (8) and (10). Finally, A_s is determined by (5). The details are given in the next section.

3 Synchrophasor Model under SSR

This section first presents a Hankel-DMD method in which two Hankel matrices are constructed to satisfy the requirement of applying DMD. Then, the equations to calculate the frequency, damping and amplitude of the SSR are analytically derived.

3.1 Hankel-Dynamic Mode Decomposition

One premise to perform DMD is that the rank of the measurement matrix needs to be no less than the number of the dominant modes [22,23]. In the case that the measurement matrix is a series of temporal synchrophasors, its rank would be one, which is insufficient for SSRPI [22]. To address this issue, the concept of Hankel matrices is used here. For the Nth measured synchrophasor $X_c(N)$, its N time-shifting historic data $(X_c(0), \ldots, X_c(N-1))$ are collected to construct two Hankel matrices $\mathbf{H_1}$ and $\mathbf{H_2}$ as follows:

$$\mathbf{H_1} = \begin{bmatrix} X_c(0) & X_c(1) & \ldots & X_c(N-L-1) \\ X_c(1) & X_c(2) & \ldots & X_c(N-L) \\ \ldots & \ldots & \ldots & \ldots \\ X_c(L-1) & X_c(L) & \ldots & X_c(N-1) \end{bmatrix} \tag{13}$$

and

$$\mathbf{H_2} = \begin{bmatrix} X_c(1) & X_c(2) & \ldots & X_c(N-L) \\ X_c(2) & X_c(3) & \ldots & X_c(N-L+1) \\ \ldots & \ldots & \ldots & \ldots \\ X_c(L) & X_c(L+1) & \ldots & X_c(N) \end{bmatrix} \tag{14}$$

where $\mathbf{H_1}, \mathbf{H_2} \in C^{L \times (N-L)}$ with $\min(L, N-L) > r$, and L is generally set smaller than $N - L$.

Actually, $\mathbf{H_1}$, stacked from overlapping elements between adjacent rows or adjacent columns with high coherence, has the property of a low-dimensional structure, as shown by the singular value (i.e., σ_i $i = 1, 2, \ldots, r$) curve of noise-free $\mathbf{H_1}$ in Fig. 1a, where the singular values are obtained by using singular value decomposition (SVD) on noise-free $\mathbf{H_1}$. The number of nonzero singular values depends on the number of dominant modes in $\mathbf{H_1}$ (or X_c). Note that Fig. 1a represents the noise-free condition. In practice, the noises in X_c would perturb small singular values in $\mathbf{H_1}$ and $\mathbf{H_2}$. In other words, the number of nonzero singular values could be more than that of the dominant mode in X_c, as shown in Fig. 1b. It is definite that $\mathbf{H_2}$ has the same property as $\mathbf{H_1}$.

With the derivation in the Appendix, the relationship of $\mathbf{H_2}$ and $\mathbf{H_1}$ is determined as

$$\mathbf{H_2} = \mathbf{A H_1} \tag{15}$$

where $\mathbf{A} \in C^{L \times L}$ is an unknown map from $\mathbf{H_1}$ to $\mathbf{H_2}$, given by

$$\mathbf{A} = \mathbf{Q \Lambda Q}^{\dagger} \tag{16}$$

where $()^{\dagger}$ is the pseudo inverse of the matrix, and $\mathbf{Q} \in C^{L \times r}$ is given by

$$\mathbf{Q} = \begin{bmatrix} a_1 & a_2 & \cdots & a_r \\ a_1\lambda_1 & a_2\lambda_2 & \cdots & a_r\lambda_r \\ a_1\lambda_1^2 & a_2\lambda_2^2 & \cdots & a_r\lambda_r^2 \\ \cdots & \cdots & \cdots & \cdots \\ a_1\lambda_1^{L-1} & a_2\lambda_2^{L-1} & \cdots & a_r\lambda_r^{L-1} \end{bmatrix}$$

and $\Lambda \in C^{r \times r}$ is given by

$$\Lambda = diag\left(\lambda_j\right), j = 1, \ldots, r \tag{17}$$

where $diag(.)$ constructs a diagonal matrix of λ_j in (11). Eqs. (16) and (17) imply that the frequency and damping of the SSR can be identified from the eigenvalues λ_j of the unknown map $\mathbf{A}$. Since Hankel matrices $\mathbf{H_1}$ and $\mathbf{H_2}$ span the dominant modes of X_c, the unknown map $\mathbf{A}$ can be approached by computationally efficient DMD.
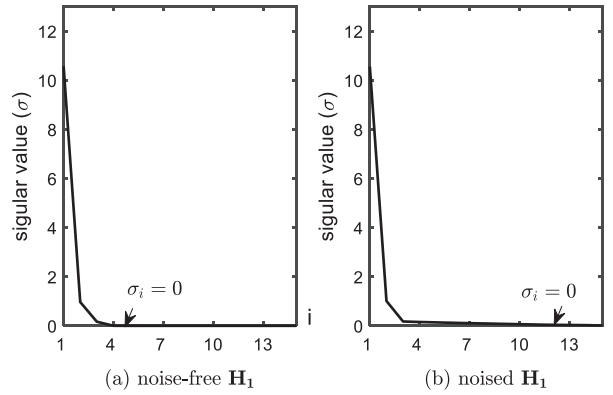

Figure 1: Singular value of $\mathbf{H_1}$ under the SSO component by using SVD. (a) Noise-free $\mathbf{H_1}$ and (b) noised $\mathbf{H_1}$

To reduce the impact of noise, reduced SVD is performed to seek the low-dimensional representation of $\mathbf{H_1}$. The SVD of $\mathbf{H_1}$ is given as

$$\mathbf{H_1} = \mathbf{U\Sigma V}^* \tag{18}$$

where $\mathbf{U} \in C^{L \times L}$ and $\mathbf{V} \in C^{(N-L) \times L}$ are the left and right singular vectors satisfying $\mathbf{UU}^* = \mathbf{I}$ and $\mathbf{VV}^* = \mathbf{I}$, $\sum \in C^{L \times L}$ is a diagonal matrix, i.e., $\Sigma = diag\left(\Sigma_1, \ldots \Sigma_i, \ldots \Sigma_L\right)$, and Σ_i is the singular value of $\mathbf{H_1}$.

By retaining the first r columns of $\mathbf{U}$ and $\mathbf{V}$, the reduced SVD gives a low-dimensional approximation of $\mathbf{H_1}$ as follows:

$$\mathbf{H_1} \approx \mathbf{U_r \Sigma_r V_r^*} \tag{19}$$

where $\mathbf{U_r} = \mathbf{U}(:, 1{:}r)$, $\Sigma_r = \Sigma(1{:}r, 1{:}r)$, and $\mathbf{V_r} = \mathbf{V}(:, 1{:}r)$ in MATLAB notation. As shown in Fig. 1, in the noise-free case, $\Sigma_{r+1} = \ldots = \Sigma_L = 0$ holds, whereas in the noisy case, $\Sigma_{r+1} > \ldots > \Sigma_L > 0$ is caused by noise. Eq. (19) thus reduces the influence of noise.

The matrix $\mathbf{U_r}$, as the proper orthogonal modes of $\mathbf{H_1}$, can project $\mathbf{A}$ into reduced dimensional space. Then, the reduced order model $\overline{\mathbf{A}} \in C^{r \times r}$ of $\mathbf{A}$ is given as

$$\overline{\mathbf{A}} \approx \mathbf{U_r^* A U_r} \tag{20}$$

Since $\mathbf{H_2} = \mathbf{AH_1}$, $\overline{\mathbf{A}}$ can be determined by solving the optimization problem in (20):

$$\min_{\overline{\mathbf{A}}} \left\| \mathbf{H_2} - \mathbf{U_r}\overline{\mathbf{A}}\Sigma_r\mathbf{V_r^*} \right\|_F \tag{21}$$

where $\|\cdot\|_F$ is the Frobenius norm, and the least-square solution of (21) is given as

$$\mathbf{A} = \mathbf{U_r^*}\mathbf{H_2}\mathbf{V_r}\Sigma_r^{-1} \tag{22}$$

where $(\cdot)^{-1}$ is the inverse of the matrix. Note that the eigenvalues for $\mathbf{A}$ and $\overline{\mathbf{A}}$ are identical [20]; thus, an eigenvalue analysis of this matrix $\overline{\mathbf{A}}$ generates the eigenvalues and dynamic modes of the system.

3.2 Calculation of SSR Parameters

The modal parameters are obtained from the eigenvalues of $\overline{\mathbf{A}}$ by using eigenvalue decomposition as follows:

$$\overline{\mathbf{A}} = \mathbf{W}\Lambda\mathbf{W}^{-1}, \tag{23}$$

where $\mathbf{W} \in C^{r \times r}$ is the matrix of eigenvectors, and Λ is constructed by the eigenvalues λ_i, given in (17). Based on the relation between λ_i and (f_i, α_i) in (8) and (10), f_i and α_i can be determined as

$$\begin{aligned} f_i &= Imag\left(\log\left(\lambda_i\right)\right)/\left(2\pi * T_r\right) \\ \alpha_i &= \mathrm{Re}\left(\log\left(\lambda_i\right)\right)/T_r \quad i = 1, 2, \ldots, r, \end{aligned} \tag{24}$$

where $Imag\left(\cdot\right)$ and $\mathrm{Re}\left(\cdot\right)$ represent the imaginary and real parts of a complex number, respectively. In this paper, we consider that the frequency range of the SSR phasor is different from that of the fundamental phasor. Moreover, according to (10), a pair of conjugated frequencies come from f_s. Based on the two rules, f_s and λ_s of SSR can be determined.

Once λ_i is estimated, the amplitudes of SSR can be obtained by first solving α_i in (12). Rewriting (12) in the matrix form gives

$$\overline{\mathbf{X}}_c = \mathbf{E}\overline{a}, \tag{25}$$

with

$$\overline{a} = [a_1, a_2, \ldots, a_r]^T,$$

$$\overline{\mathbf{X}}_c = [X_c\left(0\right), X_c\left(1\right), \ldots, X_c\left(N\right)]^T,$$

$$\mathbf{E} = \begin{bmatrix} 1 & 1 & \ldots & 1 \\ e^{j\lambda_1} & e^{j\lambda_2} & \ldots & e^{j\lambda_r} \\ \ldots & \ldots & \ldots & \ldots \\ e^{j\lambda_1(N)} & e^{j\lambda_2(N)} & \ldots & e^{j\lambda_r(N)}) \end{bmatrix} \tag{26}$$

where $(\cdot)^T$ is the matrix transpose, and $\overline{a}$ is solved in the least-square sense as follows:

$$\overline{a} = \left(\mathbf{E}^*\mathbf{E}\right)^{-1}\mathbf{E}^*\overline{\mathbf{X}}_c \tag{27}$$

where $(\cdot)^{-1}$ is the inverse of the matrix.

Finally, the amplitude A_s of the SSR component is calculated according to (10):

$$A_s = |\alpha_s|/C_s \tag{28}$$

where $|\cdot|$ is the absolute value, α_s ($1 \leq s \leq r$) corresponds to that of f_s, and C_s is calculated by (5) with the obtained f_s and α_s.

3.3 Choice of Parameters

The proposed Hankel-DMD method provides a good dynamic performance, as it uses a very short data window for SSRPI. Under noise-free conditions, the proposed method can perform well as long as the dimensions of the constructed $\mathbf{H_1}$ and $\mathbf{H_2}$ satisfy $\min(L, N - L) \geq r$ ($r = 4$ in our problem). In practice, a longer data window is desired to reduce the impact of noise, but it also degrades the dynamic performance of DMD. Through sensitive studies using both simulation and field data, this paper suggests using $N = 50$ or $N = 100$ synchrophasors X_c, i.e., a 0.5 or 1 s data window for a 50 Hz system, and L is set to be $L = N/3$.

Another parameter that affects the performance of DMD is the selection of the number of dominant modes, i.e., r. Theoretically, r should be set as 2 when SSR does not occur and 4 after SSR occurs. The cumulative percentage s_j of σ_i is used here to automatically determine the value of r, as shown in (29).

$$s_j = \frac{\sum_{i=1}^{j} \sigma_i}{\sum_{i=1}^{J} \sigma_i} \tag{29}$$

where $J = \min(L, N - L)$ and $1 \leq j \leq J$. Then, r is determined by a predefined threshold T_h, given as

$$r = \lceil j/2 \rceil \times 2, \, when \, s_j \geq T_h, \tag{30}$$

where $\lceil \cdot \rceil$ is the round up operator. Due to the impact of measurement noises, σ_i is not equal to zero when $i > r$. However, their eigenvalues are much smaller than those of the fundamental and SSR components. This indicates that j in (30) would be 1 or 2 when SSR does not occur and 3 or 4 after SSR occurs. Thus, (30) eliminates the impact of measurement noise and guarantees r to be 2 or 4 depending on the occurrence of SSR.

3.4 The Procedure of SSR Parameter Estimation

The whole procedure of the Hankel-DMD method to identify three key parameters of the SSR component, i.e., f_s, α_s and A_s, from the reported synchrophasors X_c can be summarized as follows:

- Construct two Hankel matrices $\mathbf{H_1}$ and $\mathbf{H_2}$ by using $(X_c(0), \ldots, X_c(N-1), X_c(N))$ according to (13) and (14);
- Perform SVD of $\mathbf{H_1}$, i.e., $\mathbf{H_1} = \mathbf{U\Sigma V}^*$, and determine r according to (30);
- Calculate $\overline{\mathbf{A}}$ with $\mathbf{U_r} = \mathbf{U}(:, 1:r)$, $\Sigma_r = \Sigma(1:r, 1:r)$, and $\mathbf{V_r} = \mathbf{V}(:, 1:r)$ according to (22);
- Perform eigen-decomposition of $\overline{\mathbf{A}}$ to obtain $\Lambda = diag(\lambda_j)$;
- Identify f_s and α_s according to (24);
- Identify A_s according to (27) and (28).

4 Performance Tests

This section evaluates the performance of the proposed method using both simulations and field data. Comparative studies with the InpDFT method [13] and classical Prony method are also presented.

4.1 Synthetic Data

A synthetic SSR current data was constructed as (31), where an off-nominal frequency $f_1 = 49.7$ Hz is considered

$$x(t) = 1.0 \times \cos(2\pi f_1 t + \pi/2) + x_s(t) \tag{31}$$

The parameters of the SSR components, i.e., f_s, α_s and A_s, are set as

$$\begin{cases} x_s(t) = 0 & t \in [0, 2) \\ x_s(t) = 0.2 \times e^{0.08t} \cos(2\pi \times 35.2t + \pi/6) & t \in [2, 4) \\ x_s(t) = 0.35 \times e^{-0.1t} \cos(2\pi \times 34.5t + \pi/3) & t \in [4, 10] \end{cases} \tag{32}$$

Fig. 2a shows the waveform of $i(t)$ with a sampling rate of 10 kHz. It can be seen that SSR starts at $t = 2\,s$ and its modal parameters change at $t = 4\,s$. The DFT algorithm was first performed on $x(t)$ with $N_p = 200$ (i.e., one cycle) to obtain synchrophasors X_p, and then the reported synchrophasors X_c were generated by resampling X_p with reporting frequency $f_r = 100$ Hz. Fig. 2b shows the magnitude of X_c.
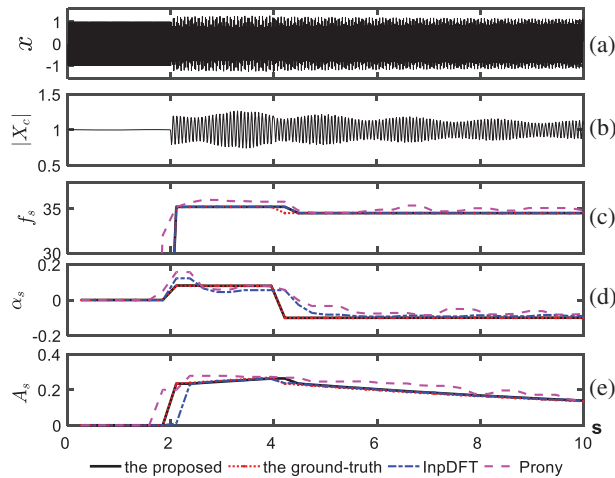

Figure 2: Synthetic SSR data and estimated results by using the proposed method and two other comparative methods for noise-free synthetic data, where each computational window applies $N = 50$ synchrophasor data. (a) Instantaneous current $x(t)$ (b) reported synchrophasor data $|X_c|$, (c) estimated f_s, (d) estimated α_s, and (e) estimated A_s

The proposed method applies a sliding window to identify the parameters of SSR, and each window contains $N = 50$ synchrophasor data (i.e., 0.5 s data). The window is shifted $N = 2$ each time, so $N = 2$ synchrophasor data overlap between two successive windows. For the synchrophasors in Fig. 2b, the estimated f_s, α_s and A_s are shown as black curves in Figs. 2c–2e, while the true values are depicted as red dot curves. To compare the proposed method with the InpDFT method and Prony method, the same sliding window scheme and window data with $N = 50$ were used in the three methods. Figs. 2c–2e also show the results obtained from the InpDFT and Prony methods, depicted as blue dot curves and magenta dot curves, respectively. As seen from the figure, the curves of the proposed method match better with the true values than those of the two comparative methods.

In another test, Gaussian noise was also added to the signal. According to our field data and those reported in the literature [24], the noises in practical PMU data are generally around a signal-to-noise ratio SNR = 45 dB. Thus, the paper considers noise with SNR = 40 dB. The results obtained from the proposed and two comparative methods are shown in Figs. 3b–3d. Since Prony is sensitive to noise, the results of Prony become worse, showing a large deviation from the ground truth under noisy conditions. The proposed method also coincides better with the true values than the InpDFT and Prony methods. Comparatively, the estimation of f_s is more accurate than that of α_s and A_s.
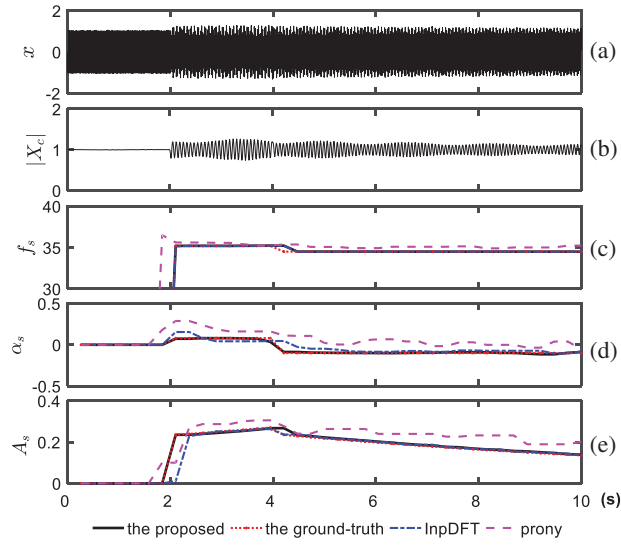
Figure 3: Synthetic SSR data and estimated results by using the proposed method and two other comparative methods for 40 dB noised synthetic data, where each computational window applies $N = 50$ synchrophasor data. (a) Instantaneous current x (t) (b) reported synchrophasor data $|X_c|$, (c) estimated f_s, (d) estimated α_s, and (e) estimated A_s

Furthermore, the mean errors of the three methods are displayed in Table 1 for two model periods, i.e., [2,4) s and (4,6) s, as shown in Fig. 2a. The mean errors E_b of each window were calculated as

$$E_b = mean \left(\frac{\left| b(t) - \tilde{b}(t) \right|}{b(t)} \times 100\% \right) \tag{33}$$

$b: f_s, \alpha_s, A_s \ t \in [2, 4) \ or \ (4, 6]$

where $mean(\cdot)$ is the mean operator and $b(t)$ and $\tilde{b}$ (t) are the true and estimated parameter values at time t, respectively. In both noise-free and noisy conditions, the proposed method achieves a higher accuracy for f_s and α_s. It is clear that the estimation of α_s from InpDFT is unacceptable. The reason is that [13] relies on DFT; thus, a longer window is required to overcome the spectral leakage issue due to the off-nominal f_1. In the case that spectral leakage does not occur, InpDFT can achieve acceptable estimation of the three parameters by using short window data.

Table 1: Mean of relative errors for the two model periods

SNR (dB)	Time (s)	Proposed method			InpDFT			Prony		
		E_{f_s} (%)	E_{α_s} (%)	E_{A_s} (%)	E_{f_s} (%)	E_{α_s} (%)	E_{A_s} (%)	E_{f_s} (%)	E_{α_s} (%)	E_{A_s} (%)
0*	[2,4)	0.00	0.18	3.39	0.26	52.89	1.88	0.37	65.73	8.58
	(4,6)	0.00	0.00	2.53	0.01	13.35	2.11	0.21	25.86	9.43
40	[2,4)	0.00	11.74	3.40	0.26	53.47	1.87	4.83	90.35	65.34
	(4,6)	0.00	2.30	2.63	0.01	31.94	1.75	4.92	200.46	64.32

Note: 0* denotes noise-free case.

4.2 Simulated SSR

The proposed method was further tested by simulated SSR data. For this purpose, a series-compensated wind farm system was modeled in MATLAB/Simulink software, as shown in Fig. 4a. A sixth-order model of the induction machine is used, with a two-mass drive train model to represent the generator shaft. Figs. 4b and 4c show the control strategies of the grid-side converter (GSC) and the rotor-side converter (RSC), respectively. Table 2 provides the key system parameters, and further details of the simulation model can be found in [25].
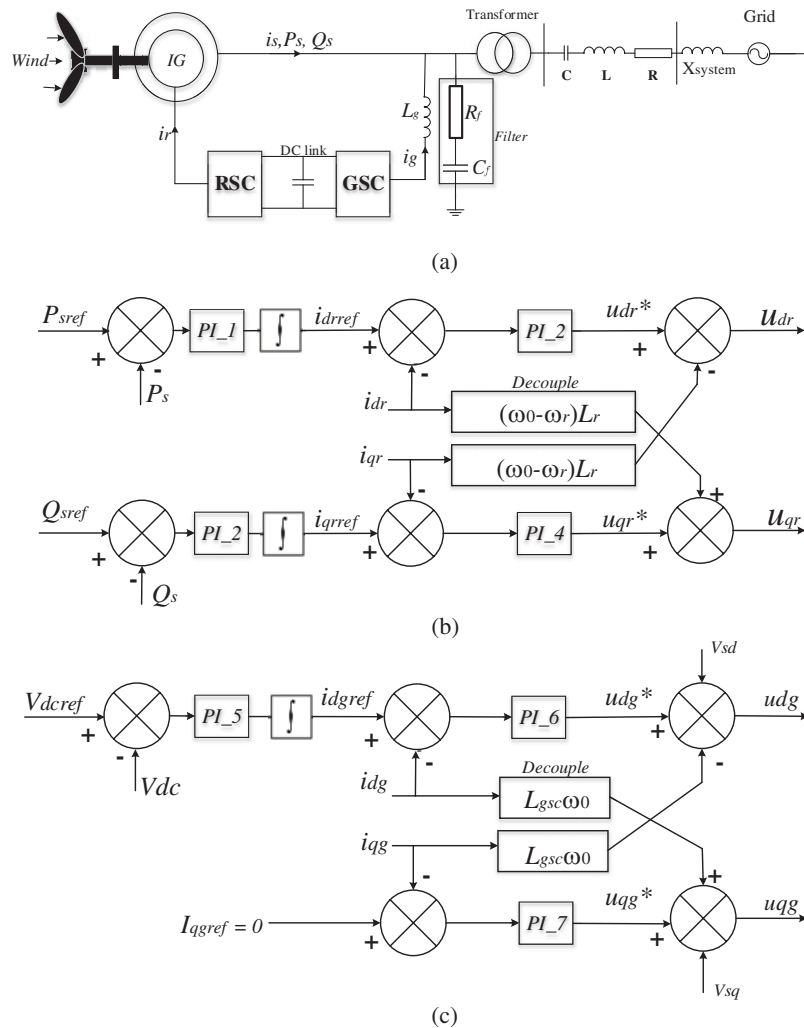
Figure 4: Simulated series-compensated DFIG-based wind farm. (a) System structure, (b) control block diagram of the RSC, and (c) control block diagram of the GSC

An SSR event is initiated at $t = 1$ s when the series compensation level of the line is increased from 0.2 to 0.3. The wind speed is initially set as 8 m/s and gradually changes to 9 m/s. The waveform of the phase A current flowing through the line and the magnitude of the corresponding synchrophasors X_c are shown in Figs. 5a and 5b, respectively. Due to the change in wind speed, the SSR mode changes, which can be clearly observed from Fig. 5a.

Table 2: System parameters

System voltage	220 kV
Equivalent system reactance, X_{system}	19.98 Ω
Transmission line inductance, L	0.3 H
Transmission line resistance, R	5.3 Ω
Series capacitance, C (20% compensation)	110 μF
Transformer voltages	220 kV/690 V

After the proposed method was performed on each window with $N = 50$ synchrophasors, the estimated SSR parameters are shown as black lines in Figs. 5c–5e. Meanwhile, the results obtained from the InpDFT and Prony methods are also shown in Figs. 5c–5e. To evaluate the accuracy of the three methods, Figs. 5c–5e show the reference values obtained from the waveform-based analysis. For the waveform-based analysis, the frequency and amplitude were directly calculated from DFT with a long-length window, while the damping was computed by the amplitude difference of two successive data windows. From Figs. 5d and 5e, it can be seen that the damping and amplitude trends obtained from the proposed method are in good agreement with the waveform-based analysis. However, the Prony method provides an unsatisfactory estimation of damping and amplitude, and the InpDFT method exhibits a poor estimation of damping due to the spectral leakage of f_1 shown in Fig. 5f.
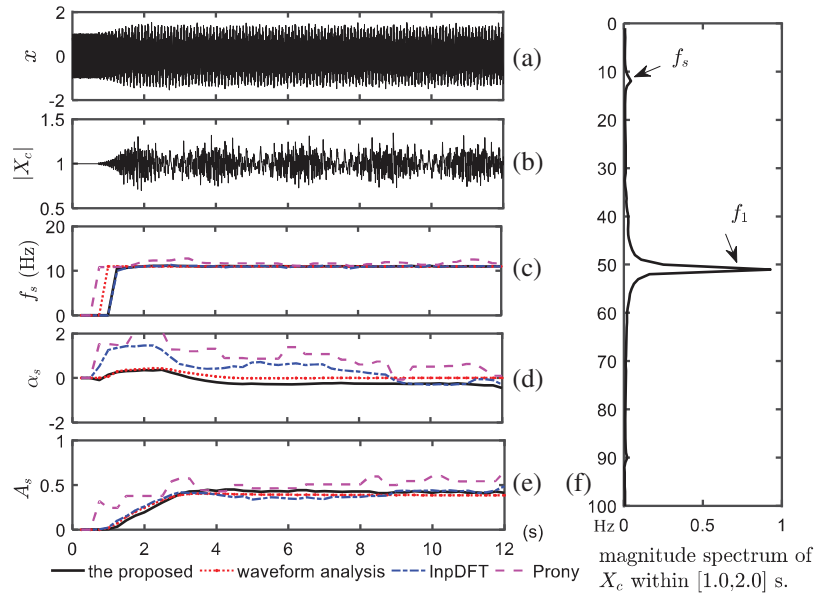

Figure 5: Simulated SSR data and results from the four methods. (a) Instantaneous current $x(t)$ (b) reported synchrophasor data $|X_c|$, (c) estimated f_s, (d) estimated α_s, and (e) estimated A_s, and (f) the magnitude spectrum of X_c within [1,1.5] s

4.3 Field Data

This subsection investigates the performance of the proposed method using practical SSR incidents that occurred in North China. Two sets of field data at different periods are used. Figs. 6a

and 7a show the waveform data provided by the fault recorder with a sampling rate of 1000 Hz, while the magnitude of the corresponding synchrophasors is shown in Figs. 6b and 7b. It can be seen that the SSR mode varies over time. The possible reasons could be the tripping of wind generators and the change in the wind speed.

The estimation results of the first case are shown in Figs. 6c–6e. Similarly, the InpDFT and Prony methods are considered for comparison, and waveform-based analysis is used as a reference. According to the results, the estimation of the proposed method matches well with the reference value, while the damping results estimated by the two comparative methods deviate from those of the proposed method and waveform analysis.
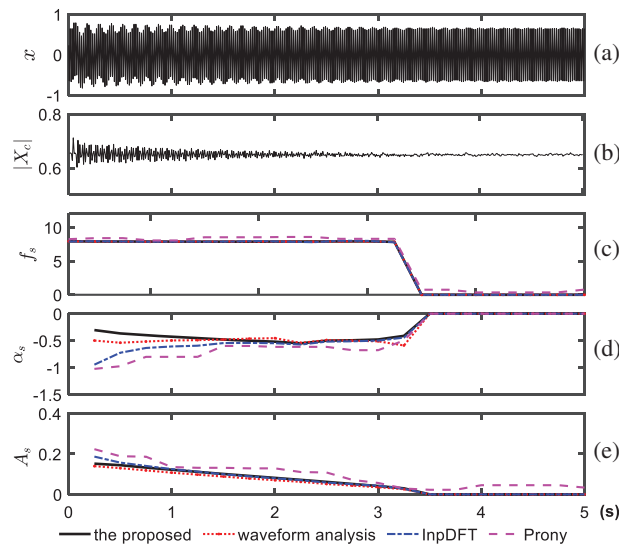

Figure 6: First set of field SSR data and estimated results from the four methods. (a) Instantaneous current x (t) (b) reported synchrophasor data $|X_c|$, (c) estimated f_s, (d) estimated α_s, and (e) estimated A_s

The estimation results of the second case are shown in Figs. 7c–7e. Different from the first case, the off-nominal condition in the second period is not severe. As a result, the curves of the estimated parameters from the proposed and InpDFT methods match well, whereas the Prony method still cannot achieve satisfactory estimation and cannot effectively capture the variation in the damping and amplitude. The estimated f_s varies between 7 and 8 Hz in Fig. 7c, which coincides with the results in [3], and the damping curves in Fig. 7d clearly show the rising and falling variation, which is consistent with the variation in the waveform amplitude. The two sets of experimental results demonstrate that the proposed method can capture the dynamic variation of the three parameters of the SSR component regardless of the spectral leakage effect.
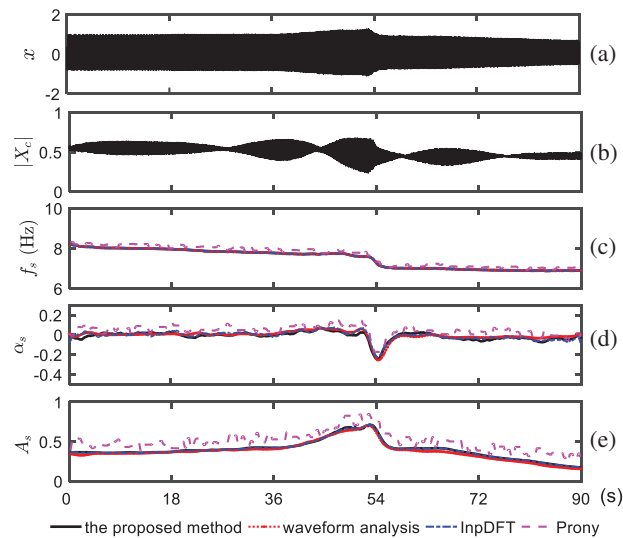
Figure 7: Second set of Field SSR data and estimated results from the four methods. (a) Instantaneous current x (t) (b) reported synchrophasor data $|X_c|$, (c) estimated f_s, (d) estimated α_s, and (e) estimated A_s

5 Conclusion

This paper presented a Hankel-DMD-based method to identify SSR parameters using synchrophasor data. Through rigorous analytical derivation, it is revealed that SSRPI can be formulated as a DMD problem. By taking advantage of the Hankel matrix, which increases the modes of the subspace, the SSR parameters can be identified using a single channel of synchrophasor data within one second. Its performance has been verified using both simulation and field data. Comparative studies also demonstrate its superiority when compared with state-of-the-art algorithms. Therefore, it is expected that the proposed method can serve as an effective tool for wide area monitoring of SSR parameters.

Conflicts of Interest: The authors declare that they have no conflicts of interest to report regarding the present study.

References

1. Suriyaarachchi, D. H. R., Annakkage, U. D., Karawita, C., Jacobson, D. A. A. (2013). Procedure to study sub-synchronous interactions in wind integrated power systems. *IEEE Transactions on Power Systems, 28(1),* 377–384. DOI 10.1109/TPWRS.2012.2204283.
2. Lawrence, C., Gross Jr, P. (2010). Sub-synchronous grid conditions: New event, new problem, and new solutions. *Proceedings of the Western Protective Relay Conference*, vol. 37, pp. 1–19. Spokane.
3. Xie, X., Xu, Z., Liu, H., Hui, L., Li, Y. et al. (2017). Characteristic analysis of subsynchronous resonance in practical wind farms connected to series-compensated transmissions. *IEEE Transactions on Energy Conversion, 32(3),* 1117–1126. DOI 10.1109/TEC.2017.2676024.

4. Liang, W., Xie, X., Jiang, Q., Hui, L., Liu, H. (2015). Investigation of SSR in practical DFIG-based wind farms connected to a series-compensated power system. *IEEE Transactions on Power Systems, 30(5),* 2772–2779. DOI 10.1109/TPWRS.2014.2365197.

5. Xie, X., Zhan, Y., Shair, J., Ka, Z., Chang, X. (2019). Identifying the source of subsynchronous control interaction via wide-area monitoring of sub/super-synchronous power flows. *IEEE Transactions on Power Delivery, 35(5),* 2177–2185. DOI 10.1109/TPWRD.2019.2963336.

6. Li, P., Xiong, L., Wu, F., Ma, M., Wang, J. (2019). Sliding mode controller based on feedback linearization for damping of sub-synchronous control interaction in DFIG-based wind power plants. *International Journal of Electrical Power & Energy Systems, 107(3),* 239–250. DOI 10.1016/j.ijepes.2018.11.020.

7. Li, P., Xiong, L., Wu, F., Ma, M., Huang, S. et al. (2022). Energy-shaping L2-gain controller for PMSG wind turbine to mitigate subsynchronous interaction. *International Journal of Electrical Power & Energy Systems, 135(3),* 107571. DOI 10.1016/j.ijepes.2021.107571.

8. Alawasa, K. M., Mohamed, Y. A. I. (2015). A simple approach to damp SSR in series-compensated systems via reshaping the output admittance of a nearby VSC-based system. *IEEE Transactions on Industrial Electronics, 62(5),* 2673–2682. DOI 10.1109/TIE.2014.2363622.

9. Netto, M., Mili, L. (2017). A robust prony method for power system electromechanical modes identification. *Proceedings of the IEEE PES General Meeting, 18,* 167–173. DOI 10.1109/PESGM.2017.8274323.

10. Ning, Z., Trudnowski, D. J., Pierre, J. W., Mittelstadt, W. A. (2008). Electromechanical mode online estimation using regularized robust RLS methods. *IEEE Transactions on Power Systems, 23(4),* 1670–1680. DOI 10.1109/TPWRS.2008.2002173.

11. Laila, D. S., Messina, A. R., Pal, B. C. (2009). A refined Hilbert-Huang transform with applications to inter-area oscillation monitoring. *IEEE Transactions on Power Systems, 24(2),* 610–620. DOI 10.1109/TP-WRS.2009.2016478.

12. Arrieta Paternina M. R., Tripathy R. K., Zamora-Mendez A., Dotta D. (2019). Identification of electromechanical oscillatory modes based on variational mode decomposition. *Electric Power Systems Research, 167(3),* 71–85. DOI 10.1016/j.epsr.2018.10.014.

13. Yang, X., Zhang, J., Xie, X., Xiao, X., Wang, Y. (2020). Interpolated DFT-based identification of sub-synchronous oscillation parameters using synchrophasor data. *IEEE Transaction on Smart Grid, 11(3),* 2662–2675. DOI 10.1109/TSG.2019.2959811.

14. Ree, J. D. L., Centeno, V., Thorp, J. S., Phadke, A. G. (2010). Synchronized phasor measurement applications in power systems. *IEEE Transactions on Smart Grid, 1(1),* 20–27. DOI 10.1109/TSG.2010.2044815.

15. Vanfretti, L., Baudette, M., Al-Khatib, I., Almas, M. S., Gjerde, J. O. (2013). Testing and validation of a fast real-time oscillation detection PMU-based application for wind-farm monitoring. *Proceedings of the First International Black Sea Conference on Communications & Networking*, pp. 216–221. Batumi.

16. Wang, Y., Jiang, X., Xie, X., Yang, X., Xiao, X. (2021). Identifying sources of subsynchronous resonance using wide-area phasor measurements. *IEEE Transactions on Power Delivery, 36(5),* 3242–3254. DOI 10.1109/TPWRD.2020.3037289.

17. Zhang, F., Cheng, L., Gao, W., Huang, R. (2019). Synchrophasors-based identification for subsynchronous oscillations in power systems. *IEEE Transactions on Smart Grid, 10(2),* 2224–2233. DOI 10.1109/TSG.2018.2792005.

18. Schmid, P. J., Sesterhenn, J. (2008). Dynamic mode decomposition of numerical and experimental data. *Journal of Fluid Mechanics, 656,* 5–28. DOI 10.1017/S0022112010001217.

19. Solaija, M. S. J., Saleem, S., Khurshid, K., Hassan, S. A., Kamboh, A. M. (2018). Dynamic mode decomposition based epileptic seizure detection from scalp EEG. *IEEE Access, 6,* 38683–38692. DOI 10.1109/ACCESS.2018.2853125.

20. Barocio, E., Pal, B. C., Thornhill, N. F., Messina, A. R. (2014). A dynamic mode decomposition framework for global power system oscillation analysis. *IEEE Transactions on Power Systems, 30(6),* 2902–2912. DOI 10.1109/TPWRS.2014.2368078.

21. Gao, B., Wang, Y., Xu, W., Yang, G. (2020). Identifying and ranking sources of SSR based on the concept of subsynchronous power. *IEEE Transactions on Power Delivery, 35(1),* 258–268. DOI 10.1109/TP-WRD.2019.2916848.

22. Tu, J. H., Rowley, C. W., Luchtenburg, D. M., Brunton, S. L., Kutz, J. N. (2014). On dynamic mode decomposition: Theory and applications. *Journal of Computational Dynamics, 1,* 291–320.

23. Filho, E. V., dos Santos, P. L. (2019). A dynamic mode decomposition approach with hankel blocks to forecast multi-channel temporal series. *IEEE Control Systems Letters, 3(3),* 739–744. DOI 10.1109/LC-SYS.2019.2917811.

24. Brown, M., Biswal, M., Brahma, S., Ranade, S. J., Cao, H. (2016). Characterizing and quantifying noise in PMU data. *Proceedings of the Power & Energy Society General Meeting*, pp. 1–5. Boston.

25. Gao, B., Torquato, R., Xu, W., Freitas, W. (2019). Waveform-based method for fast and accurate identification of subsynchronous resonance events. *IEEE Transactions on Power Systems, 34(5),* 3626–3636. DOI 10.1109/TPWRS.2019.2904914.

Appendix A. Proof of the linear combination

Let $H_1(i)$ be the ith column of $\mathbf{H_1}$ in (13), given as

$$H_1(i) = [X_c(i), X_c(i+1), \ldots, X_c(i+L-1)]^T \ (i = 0, 1, \ldots, L-1) \tag{34}$$

From (12), we obtain

$$H_1(i) = \mathbf{Q}D(i) \tag{35}$$

with

$$\mathbf{Q} = \begin{bmatrix} a_1 & a_2 & \cdots & a_r \\ a_1\lambda_1 & a_2\lambda_2 & \cdots & a_r\lambda_r \\ a_1\lambda_1^2 & a_2\lambda_2^2 & \cdots & a_r\lambda_r^2 \\ \cdots & \cdots & \cdots & \cdots \\ a_1\lambda_1^{L-1} & a_2\lambda_2^{L-1} & \cdots & a_r\lambda_r^{L-1} \end{bmatrix}$$

and

$$D(i) = \left[\lambda_1^i, \ldots, \lambda_r^i\right]^T \tag{36}$$

From (35), we can solve $D(i)$ as follows:

$$D(i) = \mathbf{Q}^\dagger H_1(i) \tag{37}$$

where $\mathbf{Q}^\dagger$ is the pseudo inverse of $\mathbf{Q}$.

Let $H_2(i)$ be the ith column of $\mathbf{H_2}$ in (14), given as

$$H_2(i) = [X_c(i+1), X_c(i+2), \ldots, X_c(i+L)]^T \ (i = 0, 1, \ldots, L-1) \tag{38}$$

Similar to (35), $H_2(i)$ is given by

$$H_2(i) = \mathbf{Q}D(i+1) \tag{39}$$

where $i = 0, 1, \ldots, L-1$. Then, we have

$$D(i+1) = \Lambda D(i) \tag{40}$$

with

$$\Lambda = diag\left(\lambda_j\right)(j = 1, \ldots, r) \tag{41}$$

by using (36).

Thus, considering (37) and (40), we can rewrite (39) as

$$H_2(i) = \mathbf{A}H_1(i) \tag{42}$$

where a linear map $\mathbf{A}$ connects the ith column data of $\mathbf{H_1}$ and $\mathbf{H_2}$, given by

$$\mathbf{A} = \mathbf{Q}\Lambda\mathbf{Q}^{\dagger} \tag{43}$$

Finally, by extending the relation of the vector in (42) to the matrix, the connection of $\mathbf{H_2}$ and $\mathbf{H_1}$ is constructed as

$$\mathbf{H_2} = \mathbf{A}\mathbf{H_1} \tag{44}$$

where $\mathbf{A}$ is a linear map from $\mathbf{H_1}$ to $\mathbf{H_2}$.